NSRRC - J0 4964 (2015)

CrystEngComm

PAPER

View Article Online
View Journal | View Issue

Cite this: CrystEngComm, 2015, 17, 8623

Core–shell nanocrystallite growth *via* heterogeneous interface manipulation†

Po-Wei Yang,[a] Yu-Ting Liu,[b] Shu-Ping Hsu,[c] Kuan-Wen Wang,[c] U-Ser Jeng,[d] Tsang-Lang Lin[a] and Tsan-Yao Chen*[ae]

Received 3rd August 2015,
Accepted 5th October 2015

DOI: 10.1039/c5ce01550b

www.rsc.org/crystengcomm

The growth of platinum shell crystals on the heterogeneous facets of ruthenium metal nanocrystals was investigated *via in situ* small angle X-ray scattering analysis. Our results illustrated that the pathway of shell crystal growth is mainly affected by controlling the incubation time prior to the thermal reduction of Pt ions by polyol radicals. For short incubation times, the shell crystal grows on the <111> radial facets and the <200> face facets of the nano-cylinder core *via* heterogeneous nucleation and crystal growth with and without assistance by transmetallation, respectively. On the other hand, severe chemical etching was observed prior to shell crystal growth after incubation for 2 hours. Consequently, the shell structure is formed from the nucleation of a PtRu alloy followed by the growth of Pt crystals. In both cases, dynamic restructuring at the core–shell interface was observed upon deposition of the shell crystal. These results enable the development of core–shell crystallites in expected configurations and with tuneable atomic structures.

Published on 06 October 2015. Downloaded on 11/12/2015 01:03:19.

Introduction

The control of the structures of nanoscale electrocatalysts (NCs) is one of the most crucial techniques for the development of fuel cell systems with high conversion efficiency and chemical stability. Following the heterogeneous catalysis principle, the development of NCs with different chemical identities and geometrical conformations is a general and effective way to meet these criteria.[1,2] From these concepts, the structural factors that decide the surface activity include the ratio of facets that are exposed to the particle surface,[3] the heteroatomic alloying, and most importantly the near-surface lattice strain of the NCs.[4–6]

The redox reactivity of bimetallic catalysts has been optimized by obtaining structures in the form of alloyed nanoparticles,[7,8] thin-films, artificial architectures (nano-tubes and flakes), and most importantly core–shell NCs (in the shape of spheres, disks, and even rods). Combining the results of density functional theory (DFT) estimations[9,10] and experimental spectral characterizations,[11–13] core–shell NCs have been proven to be the most effective, simplest, and most programmable platform for electrocatalytic applications among these structures. To optimize the activity and stability of such NCs, one can manipulate the structure/constituents of their intra-particle components in three ways, namely (1) the size, chemical identity, and shape of the core crystal,[14,15] (2) the type of heterojunction (*e.g.*, metal–metal or metal–oxide) and the extent of heteroatomic intermixing at the interface,[2,16] and (3) the thickness, identity, core coverage, and extent of surface oxidation of the shell crystal.[10,17] These factors are strongly inter-correlated and complementary, and contribute to the surface redox activity of the NCs.

Of these considerations, extensive work has been done on the structural evolution of shell and core crystals and the corresponding impact on the redox performance of core–shell NCs, including (1) changes in shell crystal thickness,[17] (2) atomic relocation at the core–shell interface upon growing the shell crystal,[17,18] (3) the identity and size of the core crystal,[14] and (4) the impact of the above three structural parameters on the valence band structure.[15,19,20] These studies disclosed most of the information about the surface reactivity of NCs and the static structure. With proper understanding of the fundamental issues, these results would likely draw a clear picture to provide strategies for developing future fuel cell electrocatalysts. Unfortunately, there is a gap between the control of NC configurations and the design of the NC

[a] *Department of Engineering and System Science, National Tsing Hua University, Hsinchu 30013, Taiwan. E-mail: chencaeser@gmail.com; Fax: +886 3 5728445; Tel: +886 3 5742671*
[b] *Department of Soil and Environmental Sciences, National Chung-Hsing University, Taichung, Taiwan. E-mail: Yliu21@gmail.com*
[c] *Institute of Materials Science and Engineering, National Central University, Taoyuan 32001, Taiwan. E-mail: kuanwen.wang@gmail.com*
[d] *National Synchrotron Radiation Research Center, Hsinchu 30076, Taiwan. E-mail: usjeng@nsrrc.org.tw*
[e] *Institute of Nuclear Engineering and Science, Hsinchu 30013, Taiwan. Fax: +886 3 5728445; Tel: +886 3 5742671*

† Electronic supplementary information (ESI) available. See DOI: 10.1039/c5ce01550b

Published on 06 October 2015. Downloaded on 11/12/2015 01:03:19.

properties, due to the lack of time resolved structural information, in particular at the core–shell interface.

Here, we demonstrate that the thickness and atomic intermixing of shell crystals (SCs) atop core crystals (CCs) are strongly affected by the atomic ratio of the SC/CC precursors, the atomic packing density of the core crystal facets, and the pre-incubation time. Without pre-incubation treatment, the shell crystals grow following the heterogeneous nucleation and crystal growth mechanism, resulting in coexisting islands and films. On the other hand, with pre-incubation treatment, the core crystal surface is exposed to a system containing a high concentration of electronegative metal ions for 2 hours. In this circumstance, the shell crystal is developed by the nucleation of a PtRu alloy followed by the growth of a Pt crystal. To the best of our knowledge, this study is the very first demonstration of monitoring the dynamic atomic restructuring of NCs at the core–shell interface upon deposition of the shell crystal by combining *in situ* small angle and wide angle X-ray scattering (S/WAXS) at a spatial resolution on the sub-atomic scale.

Experimental section

The shell crystal growth mechanisms of the experimentally obtained NCs were investigated by *in situ* small angle X-ray scattering (SAXS). The corresponding shell heteroatomic intermixing was determined by *in situ* wide angle X-ray scattering (WAXS). The impact of heteroatomic intermixing on the shell crystal growth was revealed by changing the pre-incubation (immersion) time of the Ru core or the shell metal ion concentration in the reaction system.

Synthesis of ruthenium core NPs

The ruthenium core NPs (Ru NPs) were synthesized in a solution of 100 mM ruthenium chloride ($RuCl_3 \cdot xH_2O$, 99.5%) in ethylene glycol (EG, 99.5%). In the reaction system, the concentration of stabilizer (polyvinylpyrrolidone PVP-40, MW ~42 000, 99%) was set to 10 wt%. The reaction was conducted at 160 °C for 2 h. After that, the product was cooled to room temperature for the subsequent *in situ* experiments.

In situ SAXS/WAXS characterizations

The SAXS/WAXS experiments were conducted on the BL-23A1 beamline at the National Synchrotron Radiation Center (NSRRC, Taiwan) and on the BL-12B2 beamline at Spring-8 (Koto, Japan). To achieve the proper detection resolution (from 0.008 $Å^{-1}$ to 0.6 $Å^{-1}$), the incident X-ray wavelength was selected to be 0.82667 Å (15.0 keV) and the sample to detector distance was set to be 2427.6 mm.[21] For conducting the *in situ* experiments, a sample heating cell (sample thickness = 2.7 mm) containing two X-ray transmittable windows (mica foil, 20 μm thick) and a programmable temperature controller was employed. The SAXS and WAXS signals were collected by a Pilatus 1M-F area detector (7 ms per frame, 169 mm by 179 mm) and a Mythen-3k linear detector (2.5 ms per frame, 8 mm by 18 mm), respectively. To reveal the effects of the shell precursor ($H_2PtCl_6 \cdot 6H_2O$, 99 %) concentration on the shell crystal growth mode, two SC/CC precursor ratios (1.0 and 2.0) were selected for growing the core–shell NCs, and the corresponding time resolved structure parameters were compared. The effects of interface heteroatomic intermixing on the shell crystal growth were investigated by immersing the Ru core crystal in an EG solution containing a Pt/Ru ratio of 3.0 for 2 hours prior to the *in situ* SAXS and WAXS experiments. To determine the preference of shell crystal growth for different core facets, the WAXS signal was collected simultaneously with the SAXS signal. The entire experiment was conducted under ambient atmospheric conditions. During the *in situ* experiments, the temperature of the reaction cell was controlled by a remote-controller with a heating rate of 3.1 °C min^{-1} in the ramp up region (30 to 140 °C) and then kept at 140 °C for 2 h. The thermal profile is shown by the green dashed line in Fig. 2c.

SAXS model analysis

The structure parameters of the experimentally obtained core–shell NCs were derived by fitting the corresponding SAXS spectra with a scattering function comprising the fractal cylinder aggregate[22–24] and poly core–shell cylinder[25,26] models. In this function, the SAXS spectral intensity can be expressed by the combination of the contributions of the inter-particle fractal model ($Q < 0.007$ $Å^{-1}$) and the intra-particle core–shell cylinder model ($Q > 0.007$ $Å^{-1}$) to the X-ray scattering, considering the momentum transfer of incident X-ray photons that encounter the diffused surface of a fractal aggregate, the outmost facets, and the interface in core–shell cylinder particles with polydispersion in the core size. The numerical expression is shown in

$$I(Q) = A^{FC} \cdot P(Q)^{FC} \cdot S(Q)^{FC} + A^{PCSC} \cdot P(Q)^{PCSC} \cdot S(Q)^{PCSC} \quad (1)$$

where A is the number density of the aggregates and particles. The structure factor $S(Q)$ and the particle form factor $P(Q)$ are both functions of the momentum transfer Q ($Q = (4\pi/\lambda) \times \sin(\theta)$, where θ denotes the angle between the incident and the scattered beams at a wavelength of λ). The superscripts FC (fractal cylinder) and PCSC (poly core–shell cylinder) identify the model to which the parameter belongs. The functions $P(Q)^{FC}$ and $P(Q)^{PCSC}$ are the X-rays scattered by randomly distributed cylinder "building block" particles in fractal aggregates and in core–shell cylinder particles, respectively. These cylinder particles have average and core radii R_P and R_C respectively, core length H_C, core polydispersity P, shell thicknesses at radial and facial facets of T_R and T_F respectively, volume fraction φ, and scattering length density (SLD) relative to the solvent (*i.e.*, $\Delta\rho_P = \rho_P - \rho_{solv}$, $\Delta\rho_{core} = \rho_C - \rho_{solv}$ and $\Delta\rho_{shell} = \rho_S - \rho_{solv}$, where ρ_P is the average SLD of individual scattering objects in the fractal aggregate and is determined by the core/shell precursor ratio).[24]

 This journal is © The Royal Society of Chemistry 2015

Published on 06 October 2015. Downloaded on 11/12/2015 01:03:19.

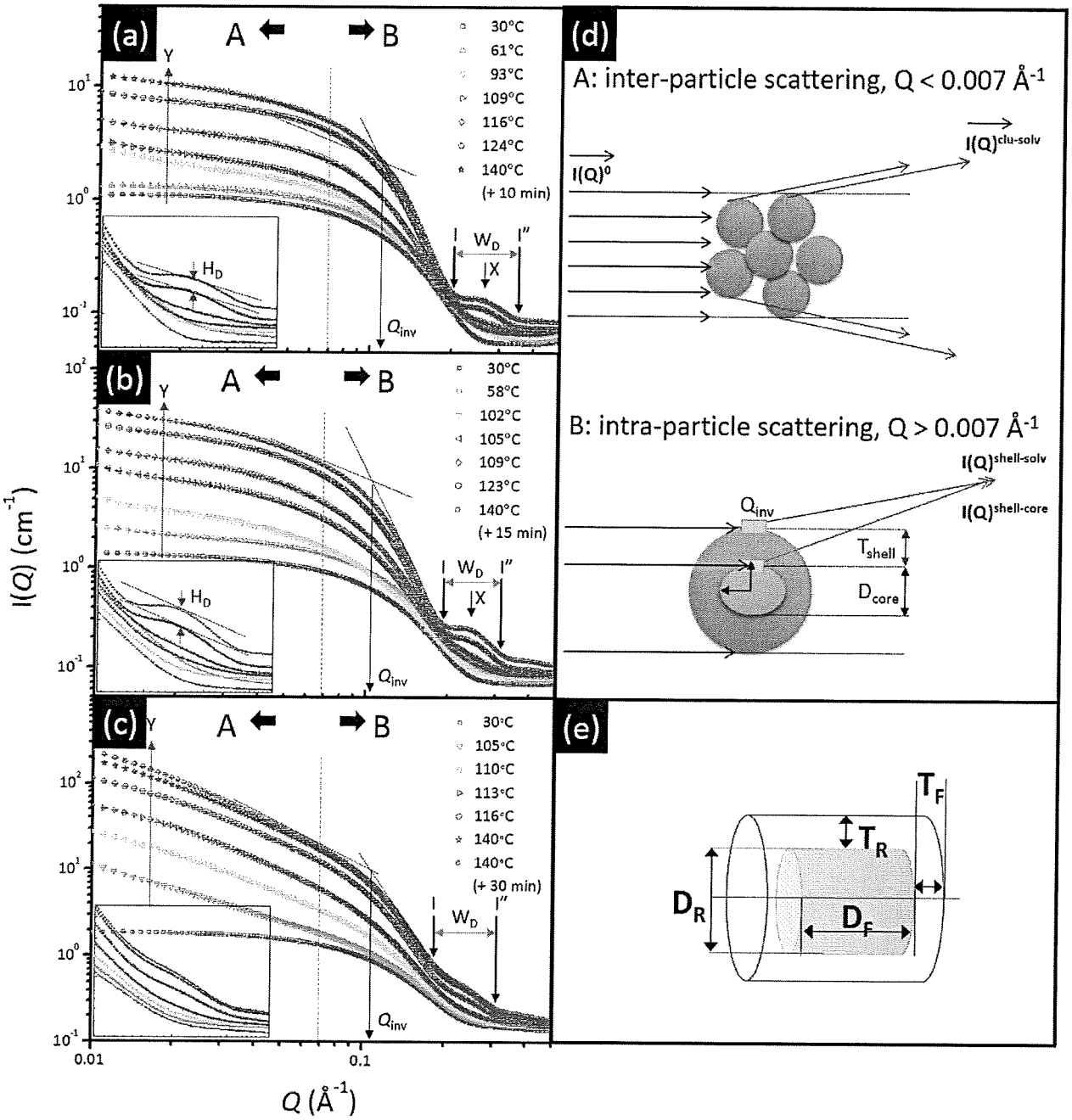

Fig. 1 *In situ* SAXS spectra of Ru core–Pt shell NCs without ((a) Pt/Ru = 1.0 and (b) Pt/Ru = 2.0) and with pre-growth transmetallation incubation reaction ((c) Pt/Ru = 3.0). (d) The models of inter- and intra-particle scattering from randomly ordered "oblate" and "core–shell oblate" nanoparticles, and (e) the scheme for the model used for the SAXS fitting analysis, where T_F refers to the thickness of the facial shell, T_R refers to the thickness of the radial shell, D_F refers to the diameter of the core crystal at a facial facet, and D_R refers to the diameter of the core crystal at a radial facet.

Results and discussion

Nanostructure evolution of core–shell NCs

The *in situ* SAXS spectra [$I(Q)$ *vs.* Q] of the core–shell NCs with SC/SS atomic ratios of 1.0, 2.0, and 3.0 are shown in Fig. 1a–c, respectively. The corresponding scheme for the X-ray scattering interference pathways and the model for fitting the SAXS spectra are shown in Fig. 1d and e, respectively. For NCs with Pt/Ru = 1.0, as indicated in Fig. 1a, five features are observed in the SAXS spectrum, including arrow Y in the low Q region (region A, in which the intensity correlates with the size of the scattering materials: diameters of particles and

Published on 06 October 2015. Downloaded on 11/12/2015 01:03:19.

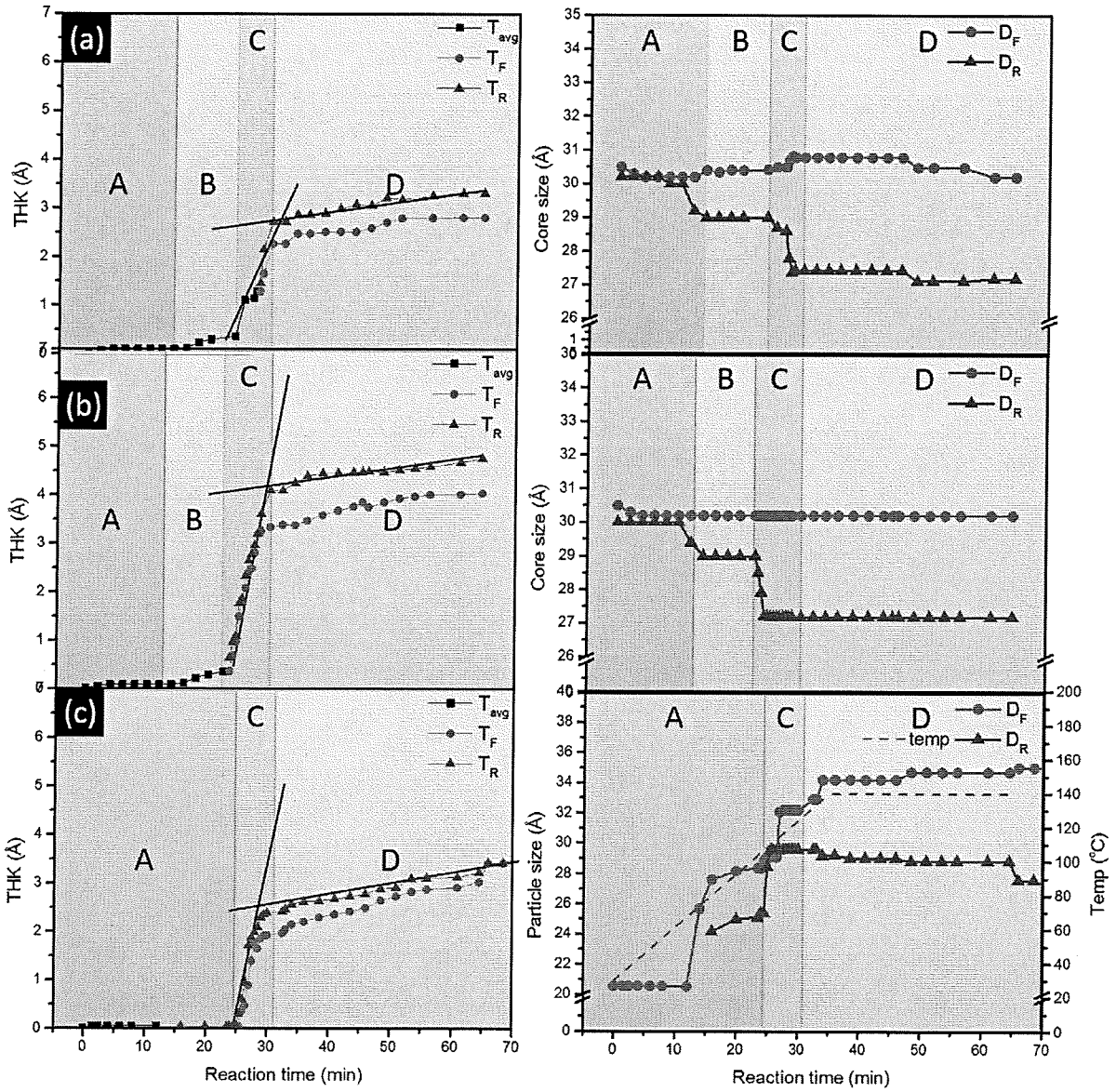

Fig. 2 SAXS determined shell crystal thickness (left side) and core diameter (right side) for the Ru core–Pt shell NPs with reaction time in ratios of (a) Pt/Ru = 1, (b) Pt/Ru = 2, (c) Pt/Ru = 3 (the corresponding polydispersities of the three NPs during *in situ* crystal growth are shown in Fig. S1†). The regions A, B, C, and D correspond to the transmetallation incubation, nucleation, shell crystal growth, and surface restructuring, respectively, during the liquid state epitaxy shell crystal growth at the heterogeneous core surface. The scheme for the scattering model of core–shell NPs is shown in Fig. 1e. The parameters T_{avg}, T_F, T_R, D_F, and D_R denote the average thickness of shell crystal (prior to the observation of distinct difference between T_F and T_R), the thickness of shell crystal at face facet, the thickness of shell crystal at radial facets, the diameter of core crystal at face facet, and the diameter of core crystal at radial facet, respectively.

the aggregates of particles), the inversion point of the spectrum (arrow Q_{inv}), and the centre (arrow X) of the first scattering hump (between I and I'') with width W_D and height H_D in the high Q region (region B). These features are affected by the geometric parameters of the polymer blended NCs. In region A, the intensity near $Q = 0$ (I_0) is caused by the contribution of incident X-rays at low contact angles to the scattering (*i.e.*, the fractal clusters of NCs in our case). Given that the experiments were conducted in dilute systems (where the metal contents were set to less than 40 mM), according to colloidal scattering theory, the increasing I_0 can be mainly attributed to the increasing cluster size ξ ($I_0 \propto \xi^6$) and slightly attributed to the packing density (fractal dimension) of the NCs in the fractal clusters/aggregates. Here, three different stages were observed upon increasing the temperature in the system. A slight increase in intensity was observed simultaneously in regions A (inter-particle interferences) and B (intra-particle interferences). This suggests increasing

 This journal is © The Royal Society of Chemistry 2015

Published on 06 October 2015. Downloaded on 11/12/2015 01:03:19.

numbers of surface defects at the core crystal surface that contribute to the scattering intensity in the entire spectrum. Given that the number density of the scattering substances (Ru core NCs) remains unchanged, such a phenomenon can be attributed to slight atomic relocation at the Ru crystal surface due to transmetallation between Pt^{4+} ions and Ru metal atoms (Ru^0) at temperatures between room temperature and 61 °C. The I_0 increased 10-fold on increasing the temperature to 138 °C. This could be a result of the increasing NC size (D_{NCs}) upon growing the shell crystal and the consequent increase in cluster size (ξ). At 140 °C, the I_0 increased with reaction time, which can be attributed to the deposition of residual Pt^{4+} and Ru^{3+} ions on the NCs. An intersection point for the tangential lines of the linear regions of regions A and B is seen in the SAXS spectrum. Its position (Q_{inv}) is a function of the curvature factors at the outmost surfaces of the scattering substances (NCs). Above Q_{inv} (~0.11 $Å^{-1}$), the X-ray scattering intensity rapidly decreased with increasing momentum transfer (Q). According to typical scattering theory, this feature coincides with the presence of out of phase scattering waves between the centre of the incident beam and the first order scattering maximum (denoted by arrow X) in the SAXS spectrum, where Q_{inv} and Q_X are inversely proportional to the size (or the aspect ratio of the longitudinal and latitudinal axes) and the shell crystal thickness (T_{shell}) of the NCs, respectively. The scattering hump (denoted by arrows I and I') originates from the interference of X-ray waveforms at the intra-particle boundaries (*i.e.*, scattering within the core crystal body and between the core–shell interface and the outmost surface of the NCs). Here, H_D and W_D are inversely proportional to the roughness of the core–shell (shell–solvent) interfaces and the polydispersity (η) of the core diameter (D_{core}) and T_{shell}, respectively. For NCs with Pt/Ru = 2.0 (see Fig. 1b), the higher rate of increase in $I(Q)_Y$ between room temperature and 58 °C indicates a larger extent of replacement of Ru^0 by Pt^{4+} ions compared to Pt/Ru = 1.0. The downshift of Q_{inv} is a direct indication of a reduction in NC curvature at the outmost surface and a reduction in the aspect ratio of the scattering substances, due to increasing T_{shell} and the uneven "chemical etching by transmetallation replacement" at the longitudinal and latitudinal facets of the Ru core. In addition, the narrowing W_D together with the increasing H_D correspond to a reduction in η for D_{core} (T_{shell}) and a reduction in the roughness of the interfaces of the shell crystal (at the outmost surface and the core–shell interface).

The effects of transmetallation on the shell crystal growth were elucidated for the NCs with Pt/Ru = 3.0. In this case, the Ru NCs were allowed to interact with Pt^{4+} ions in the reaction solution at room temperature for 2 h (pre-growth transmetallation incubation time) prior to the thermal reduction. As shown in Fig. 1c, the I_0 is decreased by ~10% for NCs with Pt/Ru = 3.0 compared to NCs with Pt/Ru = 1.0 at room temperature. This corresponds to a shrinkage of the core by 3–5% due to a certain extent of Ru dissolution (in particular the etching/removal of surface adatoms) by transmetallation pathways during the pre-thermal reduction process. On increasing the temperature to 140 °C, the I_0 is increased by more than 2 orders of magnitude. This feature can be explained by the increase in scattering length density (SLD) and crystal dimensions (particle size, D_{avg}) upon growing a high SLD Pt shell (1.32×10^{-4} $Å^{-2}$) atop the low SLD Ru core surface (9.22×10^{-5} $Å^{-2}$). If the reaction temperature (T^r) is maintained for 1.5 h, the I_0 is doubled, which can mainly be attributed to the increasing number density (due to solvent evaporation) of the NCs. Meanwhile, the intensity decay rate ($\Delta I(Q)/\Delta Q$) in region A is determined to be ~3900 ($cm^{-1} \times Å^{-1}$) and is found to be one order of magnitude higher than that for Pt/Ru = 1.0 (~250) and 2.0 (~700). Such a dramatic intensity decay illustrates the complexity of X-ray inference between waveforms that are leaving the Pt shell and Ru core regions, which is due to the formation of a thin layer Pt/Ru alloy (which slightly attenuates the intensity and randomizes the phase contrast of the scattering X-ray waveforms) at the core–shell interface prior to the growth of the Pt shell crystals for NCs with Pt/Ru = 3.0. This phenomenon is further revealed by the upshift of Q_{inv} (reduction in shell thickness) and the broadening of the scattering hump (reduction in H_D/W_D ratio) in region B.

Growth mode of shell crystals

After investigating the effects of Pt precursor concentration and transmetallation incubation time on the steric configurations of the shell components, the corresponding impact on the growth mode of the shell crystals was revealed by investigating the changes in the quantitative structural parameters of the core–shell NCs with reaction time, based on heterogeneous nucleation–growth theory and the chemical reaction kinetics. For this derivation, the intra-particle structure parameters of the core–shell NCs were determined by fitting the SAXS spectra with the scattering model in eqn (1). The obtained shell crystal thicknesses (T_F for facial facets, T_R for radial facets, and T_{avg} for the average shell crystal thickness) of NCs with Pt/Ru = 1.0, 2.0 and 3.0 as a function of reaction time and temperature are shown in Fig. 2a–c, respectively, and the corresponding core crystal sizes for these NCs are shown on the right hand side. From the results of the model analysis, we can see that the shapes of the experimentally obtained NCs were determined to be nano-disks (described in ESI†).

For NCs with Pt/Ru = 1.0 (Fig. 2a), the growth rate of the shell crystal thickness ($\Delta T_j/\Delta t$, where $_j$ denotes $_F$, $_R$, or $_{avg}$) can be divided into four regions, where regions A, B, C, and D correspond to the reaction times for transmetallation incubation (surface flattening by removing Ru adatoms), nucleation, crystal growth, and surface restructuring, respectively, upon growing the shell crystal atop the core crystal surface. In region A, only the T_{avg} can be determined at temperatures below 125 °C. This is because of incomplete coverage on both the facial and radial facets at the core surface, and thus $\Delta T_F/\Delta t$ and $\Delta T_R/\Delta t$ are indistinct. It is

Published on 06 October 2015. Downloaded on 11/12/2015 01:03:19.

important to note a decrease in D_R of ~2.2 Å (~0.9 to 1.0 atomic layers), coinciding with the preferential transmetallation at radial facets at temperatures between 60 °C and 80 °C. Further increasing the temperature to 105 °C (region B) slightly increases the T_{avg} by 0.5 Å, indicating the nucleation of subatomic Pt clusters atop the open facets of the Ru core crystal. On increasing the temperature to 140 °C (region C), the T_R and T_F are increased by 2.4 and 1.9 Å, respectively, corresponding to $\Delta T_R/\Delta t$ and $\Delta T_F/\Delta t$ of 65.6 and 52.8 (nm × 10^3 × s^{-1}), respectively. In this region, the higher growth rate implies a lower activation energy (higher surface free energy) for the adsorption and subsequent reduction of Pt^{4+} ions at the radial facets compared to the facial facets. In region D, the reaction was kept at 140 °C. The subsequent ΔT_R and ΔT_F were determined to have the same value of ~0.6 Å, resulting in $\Delta T_R/\Delta t$ and $\Delta T_F/\Delta t$ of 2.8 and 2.6 (nm × 10^3 × s^{-1}), respectively. The slow growth of the shell crystal and the reduction in the diameter of crystals at the radial facets (D_R) of 1.7 Å can be considered as indications for the reduction of residual Pt^{4+}/Ru^{3+} ions and the restructuring of adatoms at the shell crystal surface (as well as the core–shell interface), which both minimize the surface free energy of the core–shell NCs. Taking these features together, the trajectory of the shell crystal thickness (T^r) coincides with the typical diffusion controlled heterogeneous nucleation and crystal growth pathways.

For NCs with Pt/Ru = 2.0 (see Fig. 2b), the nucleation temperature is reduced by 8 °C (to 72 °C) compared to NCs with Pt/Ru = 1.0. This phenomenon can be attributed to the pile-up effects of high density Pt^{4+} ions stacking at the Ru core surface. This reduces the high diffusion barrier between the solvent and solid phases for the adsorption of Pt^{4+} ions and consequently enables the nucleation of Pt clusters at reduced temperature. In this case, $\Delta T_R/\Delta t$ and $\Delta T_F/\Delta t$ in region C are increased by ~15% to 76.4 and 64.3 (nm × 10^3 × s^{-1}), respectively, compared to NCs with Pt/Ru = 1.0. On increasing Pt/Ru to 3.0 and immersing the Ru core in Pt^{4+} solution for 2 h (see Fig. 2c), the growth of the pure Pt shell crystal does not occur below 112 °C in region A, and no nucleation step (region B) is observed. The diameters of the crystals at facial facets, D_F, and radial facets, D_R, are determined to be 20.1 and 24.0 Å, respectively. Both these two values are smaller than those for Pt/Ru = 1.0 and 2.0, indicating the occurrence of Ru dissolution *via* replacement of Ru^0 with Pt^{4+}. In this case, the growth rates of T_R and T_F are determined to be 94.7 and 84.6 (nm × 10^3 × s^{-1}), respectively, which are the highest values among the three NCs. At the Ru core facets, the shell crystals are grown by reducing the Pt^{4+} and Ru^{3+} ions with CHO: radicals at the surface facets of the Ru core crystallites. The reaction can be described by "$aPt^{4+R}_{(l)} + bRu^{3+D}_{(l)} + cCHO:_{(l)} + dRu_{(h,k,l)(S)} \leftrightarrow eRu^0_xPt^0_{1-x}@Ru_{(h,k,l)(S)}$", where Pt^{4+R}, Ru^{3+D}, and $Ru_{(h,k,l)(S)}$ denote the residual Pt^{4+} ions and dissolved Ru^{3+} ions after the nucleation reaction, and the molar volume of the solid material (*i.e.*, number density of the reaction sites (area) at the (*h*,*k*,*l*) facets of the Ru crystallites), respectively. Considering the concentrations of the reagents, the shell crystal growth rate (R_{rate}) is linearly proportional to the ideal chemical reaction kinetics and can be approximated with eqn (2):

$$R_{rate} = \xi \times k \frac{\left[Pt^{4+R}\right]^a \left[Ru^{3+D}\right]^b \left[CHO:\right]^c \left[Ru_{(hkl)(S)}\right]^d}{\left[Ru^0_x Pt^0_{1-x}@Ru_{(hkl)(S)}\right]^e} \quad (2)$$

where ξ is the surface free energy dependent crystal growth rate at a singular facet, which is dominated by the diffusion kinetics of atoms at the solid surface.[16,27,28] Since the CHO: radical is obtained from the decomposition of solvent molecules and the number density of the solid phases (*i.e.*, concentration of core crystallites "$Ru_{(h,k,l)(S)}$" in our case) remains unchanged, these values can be set as constant without affecting the reaction kinetics. When comparing the crystal growth rates at the same facets of NCs with difference Pt/Ru ratios, the effects of surface free energy can be normalized to the same value. For NCs with Pt/Ru = 2.0, the $Ru^0 \rightarrow Ru^{3+}$ dissolution rate is far slower than the thermal reduction of Pt^{4+} (*i.e.*, $[Pt^{4+R}] \gg [Ru^{3+D}]$). Hence, the R_{rate} is dominated by the concentration of Pt^{4+} with reaction order b = ~1.7. The R_{rate} for NCs with Pt/Ru = 3.0 is ~45% higher than that for NCs with Pt/Ru = 1.0 and corresponds to a reaction order of b = ~1.3. Such a low reaction order indicates a reduced correlation of $[Pt^{4+R}]$ with the R_{rate} and can again be rationalized by the competition between Ru^{3+D} and Pt^{4+R} reduction at the Ru core surfaces (*i.e.*, the formation of a PtRu alloy layer in region C prior to the growth of a pure Pt shell in region D). On increasing the reaction time to 25 min, the D_R and D_F were increased to 29.1 Å in region A. Given that no shell crystal growth was observed, this structure evolution is regarded as core crystal re-growth and can be rationalized by the minimization of total surface free energy on increasing the number of stacking layers of high surface free energy facets of Ru crystallites. Uneven re-growth was observed for D_F and D_R in the subsequent reaction regions (C and D). At the radial facets, the D_R reached the saturation size, suggesting that the thermal reduction of Ru^{3+} by CHO: radicals was at equilibrium. On the other hand, the D_F further increased to ~34 Å, indicating that the residual Ru^{3+} tends to grow at the facial facets. Such selective re-growth seems controversial, however it can be rationalized by considering the thermodynamic equilibrium of the chemical reduction reactions at crystal facets with different surface energies, as revealed by the subsequent wide angle X-ray scattering (WAXS) results (Fig. 3). These proposed mechanisms for shell crystal growth are consistent with the changes in polydispersity of the core diameter with reaction time.

Identification of the orientation of shell crystal growth

The orientations of the shell crystal facets are determined by using *in situ* wide angle X-ray scattering (WAXS) analysis. The

 This journal is © The Royal Society of Chemistry 2015

Published on 06 October 2015. Downloaded on 11/12/2015 01:03:19.

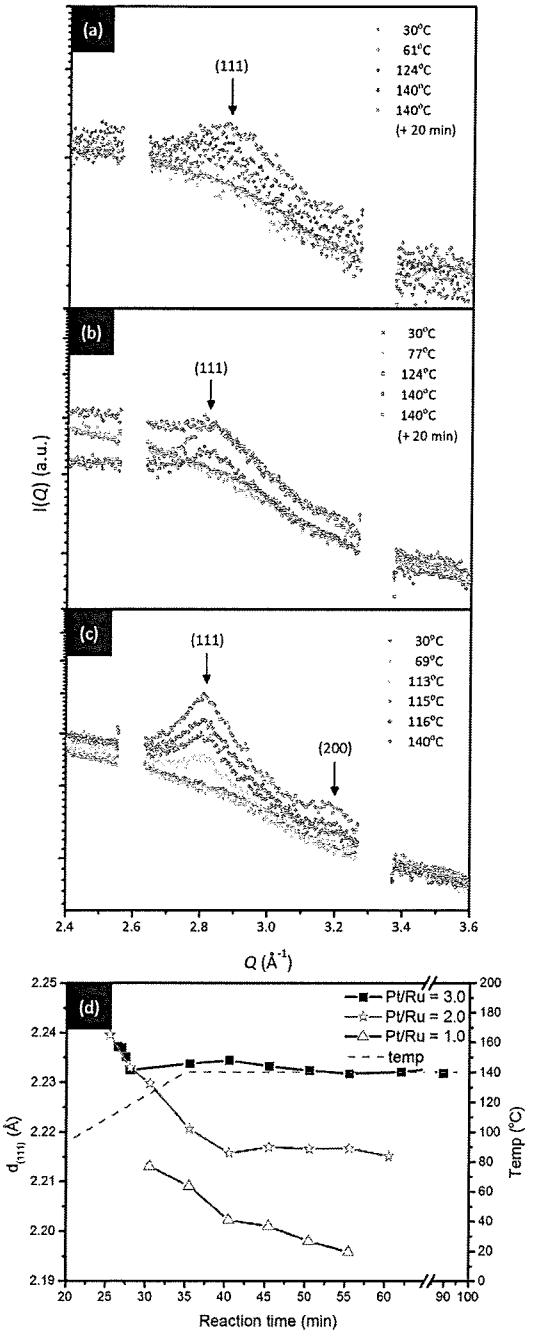

Fig. 3 WAXS spectra and corresponding average crystal size of Rucore–Ptshell NPs in atomic ratios of (a) Pt/Ru = 1, (b) Pt/Ru = 2, (c) Pt/Ru = 3 during *in situ* crystal growth, and (d) the changes of lattice space for the three NCs with reaction time.

obtained WAXS spectra of the NCs with Pt/Ru = 1.0, 2.0 and 3.0 are shown in Fig. 3a–c, respectively, while the corresponding changes in lattice space are compared in Fig. 3d. For NCs with Pt/Ru = 1.0, the presence of the diffraction line of the (111) facet at Q = 2.88 Å^{-1} indicates the formation of a sufficient volume of scattering bulk, with long-range ordering due to the transmetallation induced atomic restructuring at T^r > 124 °C.[3,29,30] Accordingly, the lattice space is determined to be 2.213 Å, which has been compressed by 2.3% compared to that of the Pt (111) facet (2.265 Å). This implies the assembly of Pt^0 atoms in pseudo alloy clusters by the confinement of Ru {1010} facets ($d_{\{1010\}}$ = 2.18 Å). The $d_{(111)}$ is further compressed to 2.195 Å on increasing the reaction time to 55 min at T^r = 140 °C. This value corresponds to an extent of Ru alloyed with Pt of ~82 at% (according to Vegard's law), however this disagrees with the thermodynamic tendency of Pt crystals to arrange homoatomically.[3] Therefore, such a dramatic difference in lattice space could only be rationalized by the combined effects of near surface alloying[31] and the compression of Pt crystals that are adjacent to Ru facets (~3.1%).[5] For NCs with Pt/Ru = 2.0 (spectra are shown in Fig. 3b), the (111) diffraction line at Q = 2.84 Å^{-1} appears at T^r = 109 °C. Compared with Pt/Ru = 1.0, T^r decreased by ~15 °C, again indicating the reduced activation energy for the growth of Pt shell crystals. In addition, the change in lattice space with increasing reaction time is similar, but occurs to a lesser extent (from 2.24 Å to 2.219 Å). This feature explains the strain relaxation at the heterogeneous interface by the restructuring of Pt into homoatomic domains and the accommodation followed by propagation of lattice displacement in the shell region with double atomic volume.[32] When Pt/Ru = 3.0 (see Fig. 3c), the $d_{(111)}$ is determined to be 2.238 Å at the beginning of (111) facet formation at 109 °C (Q = 2.82 Å^{-1}), and is then maintained at 2.232 Å when T^r > 116 °C. The slight decrease in $d_{(111)}$ of less than 0.5% to reach a stable value suggests the absence of Ru substrate confinement during the shell crystal growth and the formation of a homogeneous PtRu alloy in the shell region. It is important to note the presence of the diffraction line of the (200) facets at Q = 3.20 Å^{-1}) at T^r > 116 °C. This feature reveals that the preferential shell crystal growth has been suppressed due to replacement of Ru^0 with Pt^{4+} and the subsequent formation of a PtRu alloy, unlike the NCs with Pt/Ru = 1.0 and 2.0.

Taking the above structure evolution into account, the orientation of the shell crystals at the Ru core facets can be shown in Scheme 1 by comparing the changes in T_F (T_R) and $d_{(111)}$ with reaction time. The Ru core grows in a nano-disk shape, comprising the {0001} facial facets and the {1010} radial facets. In Scheme 1a, for NCs with Pt/Ru = 1.0 and 2.0, the shell crystals are preferentially grown at the radial facets in the {111} direction with a strong substrate compression strain. In Scheme 1c, the shell crystals are grown at the open {0001} facets with suppressed long-range ordering at the facial facets. In Scheme 1b, for NCs with Pt/Ru = 3.0, the transmetallation replacement of Ru^0 with Pt^{4+} leads to the formation of a PtRu alloy in the shell crystals at the Ru radial facets. In Scheme 1d, the high density of residual Pt^{4+} at the facial facets results in a certain extent of structural ordering at the {200} facets.

Published on 06 October 2015. Downloaded on 11/12/2015 01:03:19.

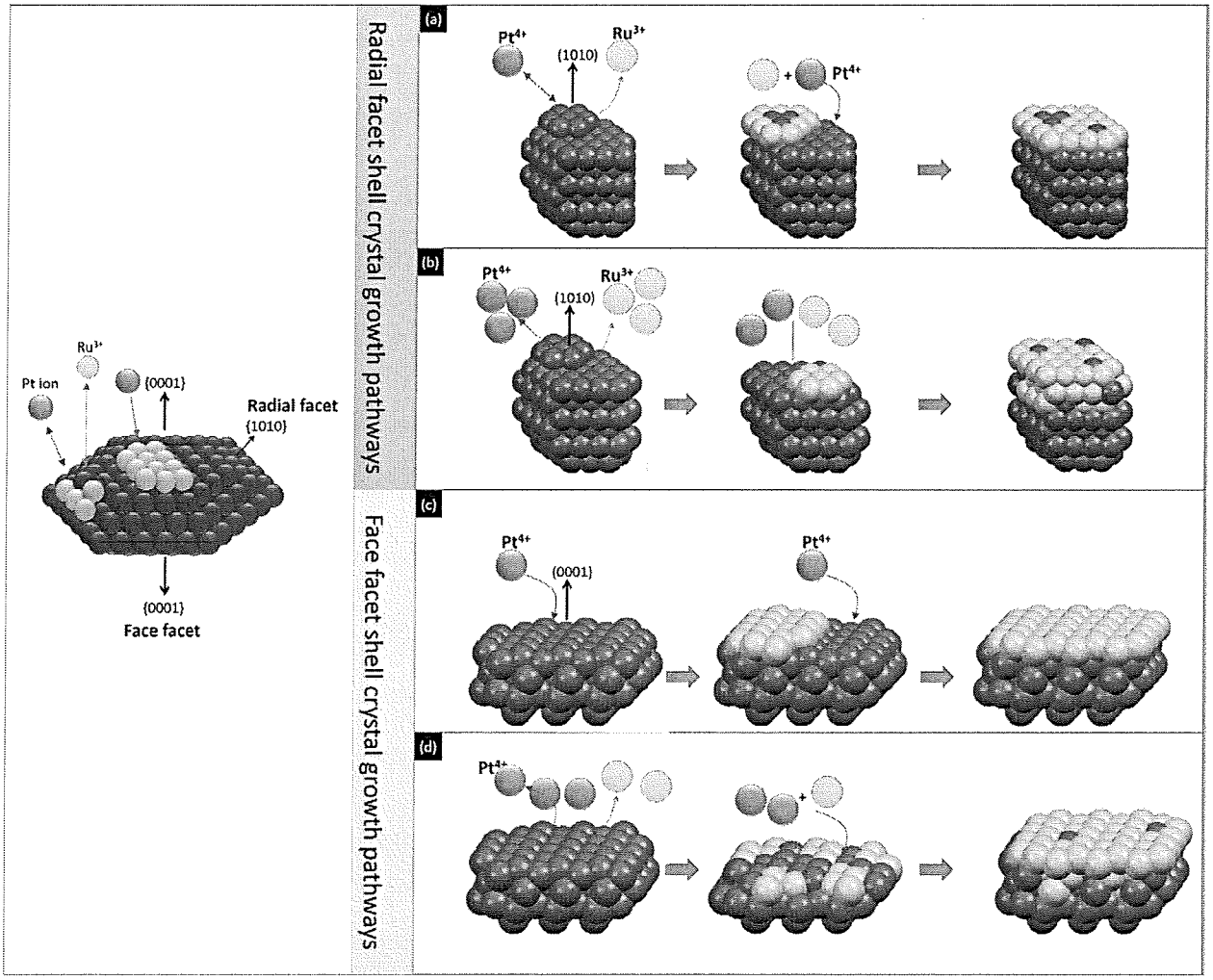

Scheme 1 Heterogeneous nucleation–growth pathways of Pt ions atop radial {1010} facets for (a) NCs with Pt/Ru = 1.0, 2.0 and (b) NCs with Pt/Ru = 3.0, and heterogeneous nucleation–growth pathways of Pt ions atop facial {0001} facets for (c) NCs with Pt/Ru = 1.0, 2.0 and (d) NCs with Pt/Ru = 3.0.

Conclusions

We demonstrated a good strategy for programming the crystal structure of core–shell NCs in expected architectures by combining the concepts of surface free energy variations of the crystal facets and spontaneous transmetallation replacement. By combining *in situ* small angle and wide angle X-ray scattering analysis, we showed that our strategy could precisely control the geometry, the lattice strain, and the composition of the shell crystals through controlling the reagent ratios, the reaction time, and the pre-incubation treatment. According to our results, the growth of the Pt shells on the Ru cores follows heterogeneous nucleation and crystal growth in four steps: (1) the transmetallation replacement of Ru^0 with Pt^{4+} during the incubation stage, (2) the nucleation of Pt nuclei at the Ru core surface, (3) the shell crystal growth at the radial and facial facets of the Ru core, and (4) the heteroatomic restructuring at the shell regions for the NCs with Pt/Ru < 2.0. In these regions, the confinement of the Ru core facets is strong and results in a progressive increase in the compression strain as the shell crystals grow. For NCs with a large extent of incubation transmetallation (Pt/Ru = 3.0), the shell crystals grow without the nucleation of Pt nuclei. In this case, the lattice strain caused by Ru confinement is slightly relaxed, which therefore results in the growth of a PtRu alloy in the shell region. Our results show the very first observation of the correlation between lattice strain and atomic restructuring in the shell region using *in situ* characterizations. We believe that such real time techniques with model analysis provide robust and effective strategies for the design of nanocrystallites with expected geometries and configurations that are capable of optimizing the performances of nano-devices in multidisciplinary applications.

Acknowledgements

The authors would like to thank the staff of the National Synchrotron Radiation Research Center (NSRRC), Hsinchu,

 This journal is © The Royal Society of Chemistry 2015

Taiwan for the help with various synchrotron-based measurements. T.-Y. Chen acknowledges the funding support from the research projects of the National Tsing Hua University, Taiwan (N103K30211 and 103N1200K3) and the Ministry of Science and Technology, Taiwan (MOST 103-2112-M-007-022-MY3).

Notes and references

1 R. R. Adzic, J. Zhang, K. Sasaki, M. B. Vukmirovic, M. Shao, J. X. Wang, A. U. Nilekar, M. Mavrikakis, J. A. Valerio and F. Uribe, *Top. Catal.*, 2007, **46**, 249–262.
2 K. Sasaki, H. Naohara, Y. Cai, Y. M. Chio, P. Liu, M. B. Vukmirovic, J. X. Wang and R. R. Adzic, *Angew. Chem., Int. Ed.*, 2010, **49**, 8602–8607.
3 T. Bligaard and J. K. Nørskov, *Electrochim. Acta*, 2007, **52**, 5512–5516.
4 P. Strasser, S. Koh, T. Anniyev, J. Greeley, K. More, C. Yu, Z. Liu, S. Kaya, D. Nordlund, H. Ogasawara, M. F. Toney and A. Nilsson, *Nat. Chem.*, 2010, **2**, 454–460.
5 S. Alayoglu and B. Eichhorn, *J. Am. Chem. Soc.*, 2008, **130**, 17479–17486.
6 F. Liu, J. Y. Lee and W. J. Zhou, *Small*, 2006, **2**, 121–128.
7 W. J. Zhou, B. Zhou, W. Z. Li, Z. H. Zhou, S. Q. Song, G. Q. Sun, Q. Xin, S. Douvartzides, M. Goula and P. Tsiakaras, *J. Power Sources*, 2004, **126**, 16–22.
8 Y.-C. Wei, T.-Y. Chen, C.-W. Liu, T.-S. Chan, J.-F. Lee, C.-H. Lee, T.-L. Lin and K.-W. Wang, *Catal. Sci. Technol.*, 2012, **2**, 1654–1664.
9 M. Watanabe, M. Uchida and S. Motoo, *J. Electroanal. Chem.*, 1987, **229**, 395–406.
10 M. P. Hogarth and T. R. Ralph, *Platinum Met. Rev.*, 2002, **46**, 117–135.
11 Y. Sun and Y. Xia, *Adv. Mater.*, 2002, **14**, 833–837.
12 C.-H. Chen, L.-S. Sarma, D.-Y. Wang, F.-J. Lai, C.-C. A. Andra, S.-H. Chang, D.-G. Liu, C.-C. Chen, J.-F. Lee and B.-J. Hwang, *ChemCatChem*, 2010, **2**, 159–166.
13 S.-Y. Huang, C. M. Chang, K. W. Wang and C.-T. Yeh, *ChemPhysChem*, 2007, **8**, 1774–1777.
14 S. Goto, S. Hosoi, R. Arai, S. Tanaka, M. Umeda, M. Yoshimoto and Y. Kudo, *J. Phys. Chem. C*, 2014, **118**, 2634–2640.
15 T.-Y. Chen, T.-J. M. Luo, Y.-W. Yang, Y.-C. Wei, K.-W. Wang, T.-L. Lin, T.-C. Wen and C.-H. Lee, *J. Phys. Chem. C*, 2012, **116**, 16969–16978.
16 T.-Y. Chen, I.-L. Chen, Y.-T. Liu, T.-L. Lin, P.-W. Yang, C.-Y. Wu, C.-C. Hu, T.-J. M. Luo and C.-H. Lee, *CrystEngComm*, 2013, **15**, 982–994.
17 T.-Y. Chen, T.-L. Lin, T.-J. M. Luo, Y. Chio and J.-F. Lee, *ChemPhysChem*, 2010, **11**, 2383–2392.
18 F.-J. Lai, W.-N. Su, L. S. Sarma, D.-G. Liu, C.-A. Hsieh, J.-F. Lee and B. J. Hwang, *Chem. – Eur. J.*, 2010, **16**, 4602–4611.
19 T.-Y. Chen, Y.-T. Liu, H. M. Nguyen, L.-J. Fan, C.-Y. Wu, T.-J. M. Luo, C.-H. Lee, Y.-W. Yang, T.-C. Wen and T.-L. Lin, *J. Mater. Chem. A*, 2013, **1**, 5660–5669.
20 C.-Y. Wu, Y.-T. Liu, P.-C. Huang, T.-J. M. Luo, C.-H. Lee, Y.-W. Yang, T.-C. Wen, T.-Y. Chen and T.-L. Lin, *Nanoscale*, 2013, **5**, 9181–9192.
21 U.-S. Jeng, C. H. Su, C. J. Su, K.-F. Liao, W.-T. Chuang, Y.-H. Lai, J. W. Chang, Y. J. Chen, Y. S. Huang, M.-T. Lee, K. L. Yu, J. M. Lin, D. G. Liu, C. F. Chang, C. Y. Liu, C. H. Chang and K. S. Liang, *J. Appl. Crystallogr.*, 2010, **43**, 110.
22 J.-M. Lin, T.-L. Lin, U.-S. Jeng, Y.-J. Zhong, C.-T. Yeh and T.-Y. Chen, *J. Appl. Crystallogr.*, 2007, **40**, s540–s543.
23 J. Teixeira, *J. Appl. Crystallogr.*, 1988, **21**, 781–785.
24 S. R. Kline, *J. Appl. Crystallogr.*, 2006, **39**, 895–900.
25 P. Bartlett and R. H. Ottewill, *J. Chem. Phys.*, 1992, **96**, 3306.
26 R. S. Justice, D. H. Wang, L.-S. Tan and D. W. Schaefer, *J. Appl. Crystallogr.*, 2007, **40**, s88–s92.
27 V. K. LaMer and R. H. Dinegar, *J. Am. Chem. Soc.*, 1950, **72**, 4847–4854.
28 J.-P. Jolivet, *Metal Oxide Chemistry and Synthesis – From Solution to Solid State*, John Wiley & Sons, Chichester, 2003.
29 S. Alayoglu, A. U. Nilekar, M. Mavrikakis and B. Eichhorn, *Nat. Mater.*, 2008, **7**, 333–338.
30 T.-Y. Chen, Y.-T. Liu, H.-S. Chen, K.-W. Wang, C.-T. Yang, T.-J. M. Luo, C.-H. Lee and T.-L. Lin, *CrystEngComm*, 2013, **15**, 3932–3942.
31 F. Besenbacher, I. Chorkendorff, B. S. Clausen, B. Hammer, A. M. Molenbroek, J. K. Nørskov and I. Stensgaard, *Science*, 1998, **279**, 1913–1915.
32 A. Schlapka, M. Lischka, A. Gross, U. Kasberger and P. Jakob, *Phys. Rev. Lett.*, 2003, **91**, 016101.

Published on 06 October 2015. Downloaded on 11/12/2015 01:03:19.